Nanoscale Advances

ROYAL SOCIETY OF CHEMISTRY

PAPER

View Article Online
View Journal | View Issue

Cite this: *Nanoscale Adv.*, 2025, **7**, 6491

Proximity effects, exchange bias and magnetic relaxation in γ-Fe_2O_3 nanoparticles

M. González de la Vega, [a] M. P. Fernández-García, [a] L. Marcano, [a] N. Yaacoub, [b] J. M. Grenèche, [b] D. Martínez-Blanco, [c] A. Adawy, [a] M. Sevilla, [d] A. B. Fuertes, [d] Jesús A. Blanco *[a] and Pedro Gorria *[ae]

Carbon-encapsulated γ-Fe_2O_3 nanoparticles (NPs) with emerging proximity effects were synthesized using a single-step solid-state pyrolysis at 750 °C. The morphology and size distribution of the NPs were investigated using high-resolution transmission and scanning electron microscopies revealing that the γ-Fe_2O_3 NPs, with an average diameter of 9 nm, are embedded in the amorphous porous carbon matrix. In addition, other trace phases (Fe_3C and metallic-Fe) were also detected through X-ray absorption spectroscopy and Mössbauer spectrometry. Moreover, the dynamics of the system was explored by means of AC susceptibility, magnetic memory and relaxation measurements, together with low-temperature exchange bias, suggesting the emergence of a spin-glass-like state that remains robust under magnetic cooling fields up to 140 kOe. These findings point to a strong exchange coupling between the spins in the ordered core and those on the disordered surface of the maghemite nanoparticles. Furthermore, the identification of robust spin-glass behaviour under high cooling fields and the demonstration of coexisting blocked and superparamagnetic phases at room temperature provide valuable insights for applications in magnetic data storage and spintronics.

Received 19th May 2025
Accepted 5th August 2025

DOI: 10.1039/d5na00493d

rsc.li/nanoscale-advances

Introduction

Although gamma ferric oxide (γ-Fe_2O_3), also known as maghemite, a name derived from the first letters of magnetite and hematite, was discovered in several mines in South Africa and California in 1927, iron oxides continue to be intensively and extensively investigated materials today, especially in their nanostructured form. The main reason for this is the broad variety of magnetic behaviours exhibited by these oxides when their size is reduced to the nanometre length-scale. The possibility of tuning their magnetic properties during the synthesis procedure enables the design of specific iron-oxide-based nanomaterials for multiple applications in different sectors including biomedicine,[1] such as magnetic hyperthermia,[2–4] magnetic resonance imaging (MRI),[5] magnetic particle imaging (MPI),[6] as well as drug delivery,[7] energy storage,[8] and environmental sustainability (*e.g.*, water remediation).[9,10] Moreover, the development of magnetic composites with large surface areas and accessible porosity would present a significant advance to improve and extend the applicability of magnetic separation techniques in fields such as catalysis and waste treatment.[11]

To fully exploit the unique characteristics of magnetic iron oxide nanoparticles (NPs) for the aforementioned purposes, low-cost production strategies based on the following features need to be developed: (i) inexpensive, stable and non-toxic materials such as magnetite (Fe_3O_4) and/or maghemite (γ-Fe_2O_3); (ii) composites whose final magnetic properties can be easily modified to ensure their separation capacity by means of electromagnets; (iii) superparamagnetic (SPM) composites with large surface areas and accessible porosity; and (iv) insulating matrices to avoid the agglomeration and uncontrolled post-synthesis oxidation of the NPs once they are formed.[12] In this regard, carbon supports have been reported to provide good protection against corrosion of NPs, in addition to the achieved chemical stability and biocompatibility.[13,14]

The encapsulation of NPs in a carbon matrix can be obtained using several fabrication routes, such as the arc discharge method,[15] chemical vapour deposition (CVD),[16,17] the solvothermal method,[18] pyrolysis procedures,[19] or other methodologies based on the precipitation of metal oxides. Among all these carbon-based synthesis procedures, our group has wide-ranging expertise in exploiting the advantages of high temperature pyrolysis, taking place on the restricted pore volume of commercial activated carbons (ACs), with the aim of obtaining

[a]*Departamento de Física, Universidad de Oviedo, Calvo Sotelo 18, 33007 Oviedo, Spain. E-mail: pgorria@uniovi.es; jabr@uniovi.es*

[b]*Institut des Molécules et Matériaux, IMMM, UMR, CNRS 6238, Le Mans Université, 72085 Le Mans Cedex 9, France*

[c]*Servicios Científico-Técnicos, Universidad de Oviedo, Fernando Bongera s/n, 33006 Oviedo, Spain*

[d]*Instituto de Ciencia y Tecnología del Carbono (INCAR-CSIC), Francisco Pintado Fe 26, 33011 Oviedo, Spain*

[e]*Instituto Universitario de Tecnología Industrial de Asturias, Universidad de Oviedo, Gijón 33203, Spain*

and studying the synthesized magnetic NPs of metals, metals/oxides and/or oxides in detail.[20–26]

It is well known that the most common iron oxide is magnetite, but when the size of the NPs is reduced to a few nanometres, the appearance of maghemite is usual. Consequently, the magnetic properties of maghemite nanoparticles have been intensively investigated since the early 2000s. Maghemite has a cubic spinel crystalline structure with a tetragonal supercell and a lattice constant of 8.33 Å. The crystal structure of maghemite can be approximated as a cubic unit cell with the composition $(Fe^{3+})_8\left[Fe_{\frac{5}{6}}^{3+}\boxdot_{\frac{1}{6}}\right]_{16}O_{32}$, where $\boxdot$ represents a vacancy.[27] As to its magnetic configuration, the Fe^{3+} moments on the tetrahedral and octahedral sites are coupled antiparallel by super-exchange interactions *via* the oxygen atoms, leaving the unpaired octahedral Fe^{3+} spins to contribute to the magnetization. As a result, the saturation magnetization of bulk maghemite is $M_s = 84$ emu g^{-1} and its Curie temperature is estimated to be around or even above 900 K.[27,28] However, these properties are altered at the nanoscale and a complex scenario arises in which disordered assemblies of maghemite NPs with a distribution of sizes and randomly oriented magnetization easy axis interact. For reference, the typical saturation magnetization (M_s) values at room temperature are approximately: 217 emu g^{-1} for α-Fe (pure iron), 92–100 emu g^{-1} for Fe_3O_4 (magnetite), 60–80 emu g^{-1} for γ-Fe_2O_3 (maghemite), ~0.2–0.5 emu g^{-1} for α-Fe_2O_3 (hematite), and 20–30 emu g^{-1} for ε-Fe_2O_3. Cementite (Fe_3C) exhibits M_s values in the range of 128–140 emu g^{-1}.[29] These comparisons underscore the relatively high magnetic response of cementite and magnetite compared to other iron oxides, and provide context for interpreting the magnetic behaviour of our carbon–iron oxide nanocomposites. These values, however, may be significantly reduced at the nanoscale due to surface spin disorder, finite size effects, and structural strain—particularly in antiferromagnetic or weakly ferrimagnetic oxides such as hematite and ε-Fe_2O_3. Therefore, when evaluating nanostructured systems, it is important to consider both the bulk properties and the additional effects introduced by reduced dimensionality.

The complexity stems from the combination of: (i) collective behaviour due to interparticle interactions (dipole–dipole and/or exchange interactions if the NPs are in close contact); (ii) surface effects caused by uncompensated, canted spins and broken bonds; (iii) intraparticle phenomena (*e.g.* volume, surface and exchange anisotropy)[30] and (iv) finite size effects (*i.e.* truncation of the magnetic correlation length). As a result of all these effects, the magnetic properties of the surface can even govern the magnetism of the inner core, reducing the magnetization, increasing the effective magnetic anisotropy, and giving rise to spin canting or SG effects.[31]

On the other hand, the exchange bias (EB) effect appears in systems with ferromagnetic (FM)/antiferromagnetic (AFM) or ferrimagnetic (FiM) interfaces when they are cooled from above the T_N of the AFM phase (or T_c in the case of the FiM phase) under an applied magnetic field.[27,32–36] It generally manifests as a horizontal shift of the hysteresis loop along the field axis and an enhancement of the coercive field, H_c. Due to the interest of this phenomenon with regard to applications in magnetic sensors and data storage, EB has been experimentally and theoretically scrutinised since the early 1970s.[29,37] In thin films and/or core/shell NPs, the EB has been ascribed to exchange coupling moments at the FM/AFM interface,[38,39] or to disordered interfacial spins or spin clusters.[40,41] More recently, it has been reported that the EB effect can also be observed in FM/SG interfaces. The EB effect is sensitive to increases in the surface/core ratio when the size of the NPs is reduced or their morphology is modified (*i.e.* spheres, cubes, octopods, flowers, *etc.*).[42] As the EB depends strongly on the thermal and magnetic histories, magnetic measurements typically track changes in the initial and final cooling temperatures and training (*i.e.* the number of consecutive loops after cooling).

In this article, we report on detailed microstructural characterization in addition to the magnetic behaviour investigation of γ-Fe_2O_3 NPs with a mean diameter less than 10 nm synthesized by a pyrolysis method taking place in the restricted porous microstructure of AC carbons. The combination of high-resolution transmission electron microscopy (HRTEM), X-ray absorption near-edge structure (XANES), extended X-ray absorption fine structure (EXAFS) and Mössbauer spectrometry revealed that, in addition to maghemite, a small amount of cementite and almost undetectable metallic iron are present in the sample. Moreover, the dynamics of the system was explored by means of AC susceptibility, magnetic memory and relaxation measurements, together with low temperature exchange bias suggesting a low temperature spin-glass-like (SG) state robust enough to persist under magnetic cooling fields up to 140 kOe. These findings can be interpreted in terms of maghemite NPs with a strong exchange coupling between the spins of the ordered core and those located at the disordered surface of maghemite NPs.

Experimental

Commercial activated carbon (AC) supplied by Osaka Gas (Japan) with a large Brunauer–Emmett–Teller (BET) surface area of 2350 m^2 g^{-1}, a high pore volume of 1.47 cm^3 g^{-1} and a porosity composed of mesopores with diameters up to 6–7 nm and centred around 2.5 nm was used to prepare the Fe-oxide NPs. The synthetic method to fabricate the magnetic NPs is based on pyrolysis in the restricted volume formed by the AC porosity. As in typical fabrication, 0.59 g AC was impregnated to the moisture with a solution of water (1 g), sucrose (0.5 g) and iron nitrate (0.44 g). The impregnated sample was dried, then heat-treated under an N_2 atmosphere and kept at 750 °C for 3 hours. Finally, the sample was then cooled in a controlled atmosphere to room temperature and passivated with a small stream of air to stabilize it. The Fe content of the sample was subsequently determined by thermogravimetric analysis (TGA) in air, obtaining a value of 7.3 wt% Fe.

Transmission (TEM) and high-resolution transmission (HRTEM) electron microscopy images were obtained using

a JEOL 1011 and a JEOL-JEM-2100F microscope operating at 180 kV and 200 kV, respectively. The samples were prepared by formulating a powder suspension in pure ethanol and depositing 5 μL on carbon-coated copper grids, which were then left to dry at room temperature.

The crystal structure of the Fe NPs was analysed using room temperature X-ray powder diffraction (XRD) patterns collected on a high-resolution Seifert XRD 3003 and Panalytical diffractometers in Bragg–Brentano geometry operating at 45 kV and 40 mA, using Mo and Cu K_α radiation, respectively ($\lambda_{Mo} = 0.7107$ Å and $\lambda_{Cu} = 1.5418$ Å).

X-ray absorption structure measurements (XANES and EXAFS) of the sample were carried out at room temperature and atmospheric conditions at the XAFS beamline (11.1) of the Elettra Synchrotron in Trieste, Italy. The monochromator used in the experiment was a double crystal of Si(111). The Fe K-edge absorption spectra were collected in the transmission mode using ionization chambers as detectors.

For the measurements, homogeneous layers of the powdered samples were prepared by spreading the powder over an adhesive tape. The thickness and homogeneity of the samples were optimized to obtain the best signal-to-noise ratio. To improve data reliability, 3 spectra were recorded for the sample. The energy edge of each sample was carefully calibrated by simultaneously recording a XANES spectrum of an Fe foil placed after the sample. Under these conditions, the edge position of the sample can be determined with an accuracy of 0.2 eV. Furthermore, a linear combination of different Fe K-edge XANES sub-spectra was compared with the XANES measurement of the sample. These XANES measurements correspond to a maghemite standard and α-Fe foil, a $Fe_{50}Ni_{50}$ sample with an FCC crystal structure and a lattice parameter of 3.592 Å (close to that of the γ-Fe phase).[43] In addition, an Fe_3C XANES spectrum was provided by Dr Lusegen Bugaev.[44]

The normalized XAFS functions, $\chi(k)$, were extracted from the raw data using the standard procedure. The absorption above the edge was extracted using a cubic spline in the k range $2.5 \leq k \leq 14.5$ Å^{-1}. The origin of the k space was taken at the inflection point of the absorption edge. The Fourier transforms of $\chi(k)$ were performed in the k range $2.5 \leq k \leq 14.5$ Å^{-1} with a k^2 weight and a Hanning window function. The contribution of the nearest neighbours to the EXAFS function was isolated by selecting the first peaks of the Fourier transform ($1 \leq R \leq 3.5$ Å) and using the standard Fourier filtering technique. The overall scale factor, $S_0{}^2$, was fixed at 0.8. The Debye–Waller factors, σ^2, were assumed to be uniform across all paths, confined within physically feasible ranges between 0.0075 and 0.01 Å^2. All data were treated using Athena and Artemis software from the Iffefit package.[45]

^{57}Fe Mössbauer spectra were recorded at 300 and 77 K, using a constant acceleration spectrometer and a ^{57}Co source diffused in an Rh matrix. The transducer was calibrated using a α-Fe foil at 300 K. The sample consisted of a thin homogeneous layer of powder containing about 5 mg Fe per cm^2 to optimize the counting rate (registration time) and avoid thickness effects. The values of the hyperfine parameters were refined using the MOSFIT least-squares fitting procedure (F. Varret & J. Teillet, unpublished MOSFIT program, Le Mans Université, France). The description of the hyperfine structures results from quadrupolar doublets and magnetic sextets composed of Lorentzian line shapes. The isomer shift (IS) values are given relative to that characteristic of the α-Fe spectrum at 300 K. The percentage of each Fe species was derived from their relative spectral areas, assuming the same value of the *f*-Lamb–Mössbauer factors for the different components.

The temperature and applied magnetic field dependences of the magnetization, $M(T)$ and $M(H)$ curves, respectively, were measured using a Quantum Design PPMS-14T magnetometer with the vibrating-sample (VSM) option. First, the sample was cooled in zero field (ZFC) from 300 K down to 2 K. Then, the magnetic field was applied and kept constant. The magnetization was measured at fixed temperatures on heating from 2 to 340 K, $M_{ZFC}(T)$ curve, and cooling down from 340 to 2 K, $M_{FC}(T)$ curve. The hysteresis loops were recorded after cooling the sample from 300 K with [$M(H)$ @ FC] and without [$M(H)$ @ ZFC] an applied magnetic field. The value of the exchange-bias field, H_{EB}, is defined as the horizontal shift of the central point of the $M(H)$ loop measured at a given H_{cool}, relative to the $H_{cool} = 0$ loop, *i.e.* $H_{EB} = -\frac{H_{right} + H_{left}}{2}$, where H_{right} and H_{left} are the points where the loop intersects the field axis. For the training effect of the exchange bias measurements, the system was cooled under a magnetic field of 5 kOe from 300 to 4 K, where the magnetic field was cycled several times.

The dynamic magnetic properties were investigated by measuring the real (χ') and imaginary (χ'') parts of the magnetic AC susceptibility in the 2–300 K range for a set of seven different values of the frequency (f = 200, 500, 1000, 2000, 5000 and 10 000 Hz).

Magnetic memory experiments were carried out according to FC protocols. In the FC memory effect protocol, the magnetization was measured while the sample was cooled from 340 K under a constant magnetic field of 100 Oe with intermittent stops at 100, 80, 60, 40 and 20 K. At each stop, the field was switched off for 3 hours and subsequently switched on to 100 Oe before cooling was resumed.

For the magnetic relaxation measurements, the system was cooled from 340 to 30 K in a zero field. Then, a field of 100 Oe was applied and kept constant, and the magnetization was recorded for 3 hours (t_1). Then, while maintaining the magnetic field constant, the system was cooled to 20 K and the magnetization was measured for 3 hours (t_2). Finally, the system was warmed to 30 K and the magnetization was recorded for 3 hours.

Results and discussion

Crystalline structure

Room temperature X-ray diffraction (XRD) patterns (Fig. S1) show broad peaks superimposed onto diffuse scattering associated with the predominant (90%) amorphous carbon matrix. The peaks can be indexed as those corresponding to the maghemite crystal structure (space group $P4_132$). The fact that the peaks are not sharp Bragg reflections gives an idea of the

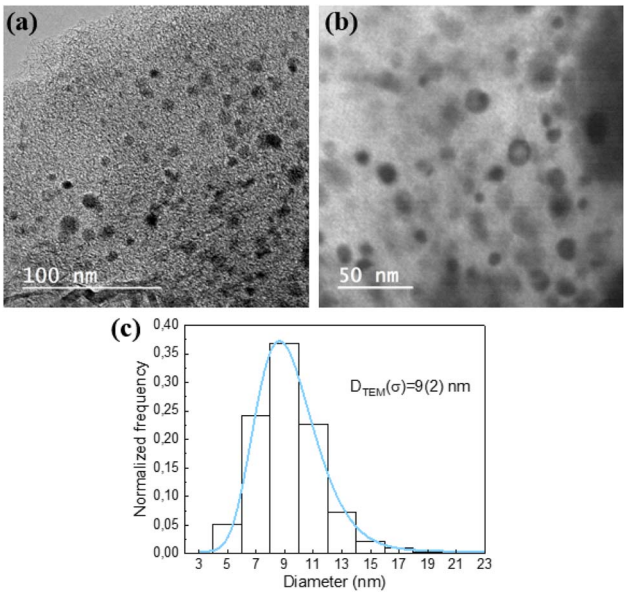

Fig. 1 (a and b) Bright-field images of the NPs revealing their random distribution in the porous carbon matrix. (c) Histogram of the NP diameter together with the best-fit log-normal distribution (blue solid line), characterized by the mean diameter (D_{TEM}) and standard deviation (σ) parameters.

small size of the NPs. Given the synthesis process in amorphous carbon matrices and the pyrolysis temperature of 750 °C being reached, the presence of metallic Fe and cementite (Fe_3C) in low percentages cannot be excluded.[44] However, low percentages or very thin coating layers on the nuclei of the NPs might be below the minimum XRD coherence length required to be detected. As a result, other detection methods are needed to properly achieve the identification of phases present in small volume fractions.

Microstructure and morphology

Bright-field and high-resolution lattice fringe images (HRLFI) revealed the semi-spherical morphology [Fig. 1(a) and (b)] of the NPs, which are randomly distributed in the AC matrix (grey surface in the background of the TEM images). Analysis of the nanoparticle size distribution was carried out by measuring the diameters of more than 2000 NPs in several images using the ImageJ programme and creating the histogram to model the diameter of the NPs using a log-normal function. These results reveal that the NPs have a broad size distribution [Fig. 1(c)], characterized by a mean NP diameter (D_{TEM}) of 9.4(0.1) nm and a standard deviation (σ) of 2.2(0.7) nm. These small sizes, together with the reduced Fe content determined by TGA

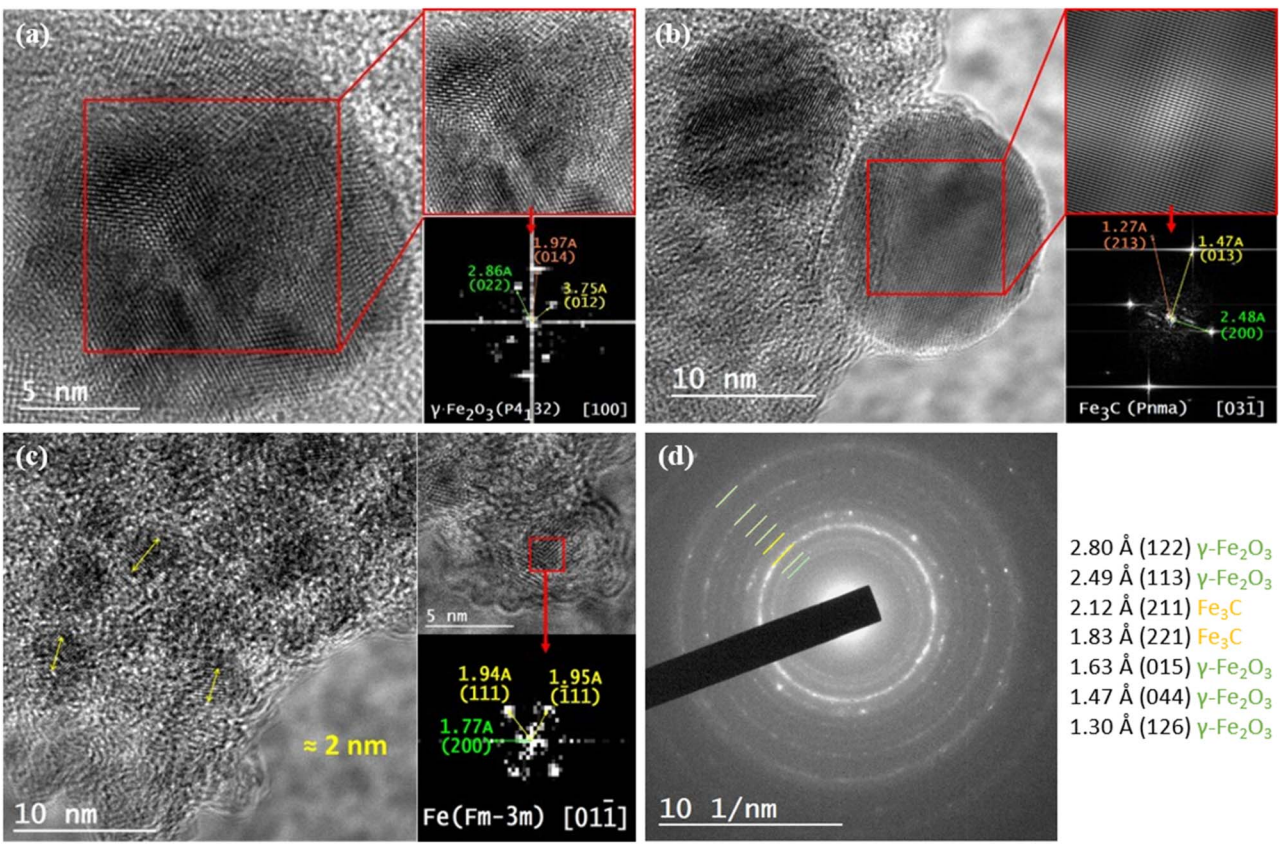

Fig. 2 HRTEM images for individual γ-Fe_2O_3 (a), Fe_3C (b) and Fe (c) NPs as determined from the crystallographic analysis of the processed images of the red-squared area and fast Fourier transform (FFT) of each image. (d) SAED pattern of an area containing different NPs embedded in the carbon matrix showing diffraction rings indexed to interplanar distances associated with γ-Fe_2O_3 and Fe_3C crystal structures (see text for more details).

(7.3 wt% Fe), could explain why they were weakly detected by XRD.

The crystallographic analysis of the HRLFI (Fig. 2) confirmed the presence of γ-Fe_2O_3 [Fig. 2(a)] in addition to other phases [Fe_3C, see Fig. 2(b) and small Fe-metallic NPs, see Fig. 2(c)] that were not detected using XRD, indicating their small percentage compared to the former. Fig. 2(a) shows a high-resolution lattice fringe image for a γ-Fe_2O_3 NP as determined from crystallographic analysis of its processed image of the red squared area and its fast Fourier transform (FFT), revealing crystallographic planes in line with the [100] zone axis of a cubic crystal belonging to space group $P4_132$.

Fig. 2(b) shows a high-resolution lattice fringe image for a Fe_3C NP as shown with its autocorrelation for the red squared area and crystallographic analysis that revealed that the crystallographic planes corresponding to the zone axis $[03\bar{1}]$ of an orthorhombic crystal belonging to the space group *Pnma*. Fig. 2(c) reveals that a very small portion of relatively much smaller NPs was detected in the carbon matrix with a diameter ≈ 2 nm. Their crystallographic analysis suggests that they belong to Fe, as shown by the FFT of the squared region (the zone axis $[01\bar{1}]$ of a cubic crystal with $Fm\bar{3}m$ space group). Selected area electron diffraction (SAED) of the carbon matrix embedding hundreds of the obtained NPs confirmed their crystallinity and also proved the presence of maghemite and cementite, identified by Bragg diffraction rings corresponding to Miller indices (122), (113), (015), (044), (126); and (211), (221), respectively [see Fig. 2(d)]. It is worth mentioning here that no turbostratic carbon layer around the maghemite NPs was observed in the HRLFI. Consequently, we can conclude that, in contrast to Ni,[22] sucrose could not be graphitized on the surface of the iron NPs but might have been responsible for the existence of cementite.

X-ray absorption near-edge structure (XANES)

To better understand the local structure of the samples, we performed X-ray absorption spectroscopy, encompassing both X-ray absorption near edge structure (XANES) and extended X-ray absorption fine structure (EXAFS) analyses. Fig. 3(a) shows the comparison of the Fe K-edge XANES spectra from the sample and a maghemite standard, thus providing further confirmation of the predominance of iron oxide as suggested by XRD and HRTEM analyses.

The edge positions of the sample align precisely with those of maghemite, clearly indicating the oxidation state of the absorbing atom and confirming that the prepared sample predominantly consists of a pure Fe^{3+} compound.

However, some differences are observed between our sample and maghemite standard in the pre-edge region (approximately 10 eV below the edge position), the white-line intensity and the post-edge region of the XANES spectra [see Fig. 3(a)]. The pre-edge peak corresponds to a 1s to 3d transition, which is typically forbidden by dipolar selection rules. The intensity and width of this peak are highly sensitive to the symmetry around the absorbing atom.[46] In particular, the pre-edge peak of our sample exhibits a higher intensity than that of maghemite,

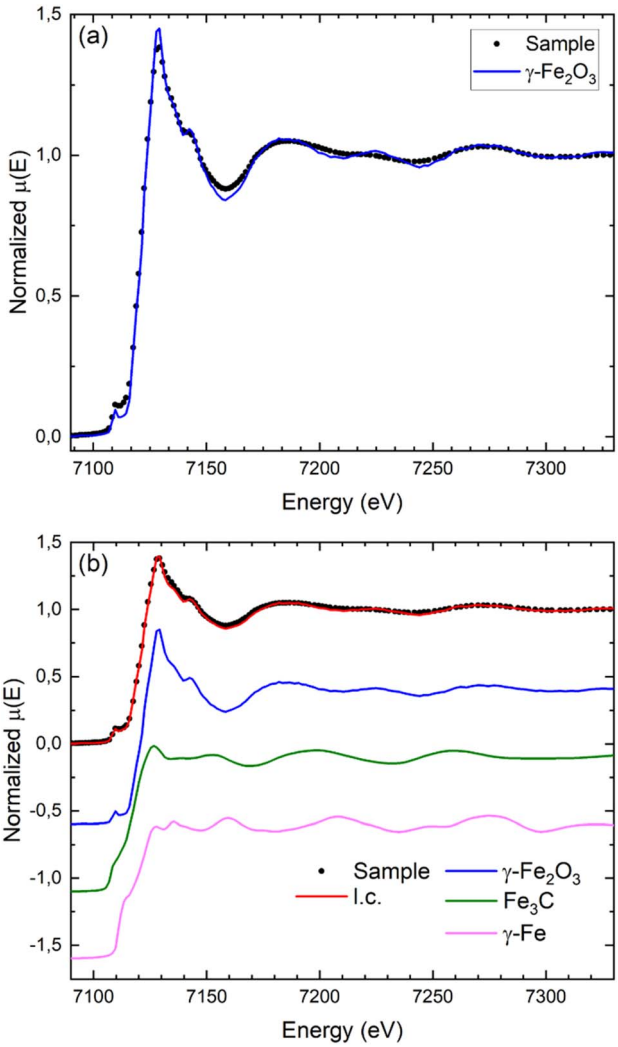

Fig. 3 (a) Comparison of the normalized XANES spectra obtained from our sample with maghemite. (b) Linear combination fit of the sample with maghemite (87%), Fe_3C (12%) and γ-Fe (1%).

accompanied by a broader shape that smoothly merges with the edge. These characteristics suggest the presence of a distinct symmetry around the Fe-absorbing atoms. Similarly, above the edge, the XANES spectra of our sample show pronounced oscillations that differ from those observed in maghemite. These discrepancies confirm the coexistence of predominant maghemite with other Fe phases, *i.e.*, the experimental K-edge XANES spectrum requires additional components in addition to maghemite to accurately reproduce the observed features. To this end, a linear combination (l.c.) fit was performed, considering the Fe K-edge XANES spectra of maghemite, cementite and γ-Fe.

The best fit was achieved in fact by considering the coexistence of the three phases: γ-Fe_2O_3, Fe_3C and a small amount of γ-Fe. As expected, maghemite was identified as the dominant phase, up to 87(3)% of the sample, while Fe_3C contributed approximately 12(3)%. The remaining 1(3)% corresponds to γ-Fe. Note that the associated error in determining the phase percentages was estimated at 3%.

Consequently, although a subtle contribution from γ-Fe can be deduced from the fitting analysis, the estimated contribution is within the range of error. Therefore, the linear combination considered with maghemite, γ-Fe and Fe_3C reproduces the shape, energy position and intensity ratio of the experimental XANES spectrum of the sample allowing us to conclude that the NPs are almost completely maghemite, although the reduction of this Fe-oxide has already started at a pyrolysis temperature of 750 °C.

Extended absorption fine structure (EXAFS)

To gain quantitative information about the detected multiple phases within the synthesized sample, we also conducted extended X-ray absorption fine structure (EXAFS) analysis. Fig. 4 shows the EXAFS spectra, $\chi(k)$, and the modulus of the Fourier transform, $\Phi(R)$, at the Fe K-edge obtained for the sample. The EXAFS spectra extend up to $k = 14.5$ Å^{-1} with a high signal-to-noise ratio. Even when the whole k-range was used in the EXAFS fitting, for the sake of a straightforward qualitatively comparison, the Fourier transform $\Phi(R)$ presented in Fig. 4(b) was performed over the k range 2.5 Å$^{-1} \leq k \leq 14.5$ Å^{-1}, using a Hanning window and a k^2 weighting factor to compensate the amplitude decay at high k values. With this k range, we can distinguish scatterers with a $\Delta R \geq \frac{\pi}{2\Delta k} = 0.13$ Å.[47]

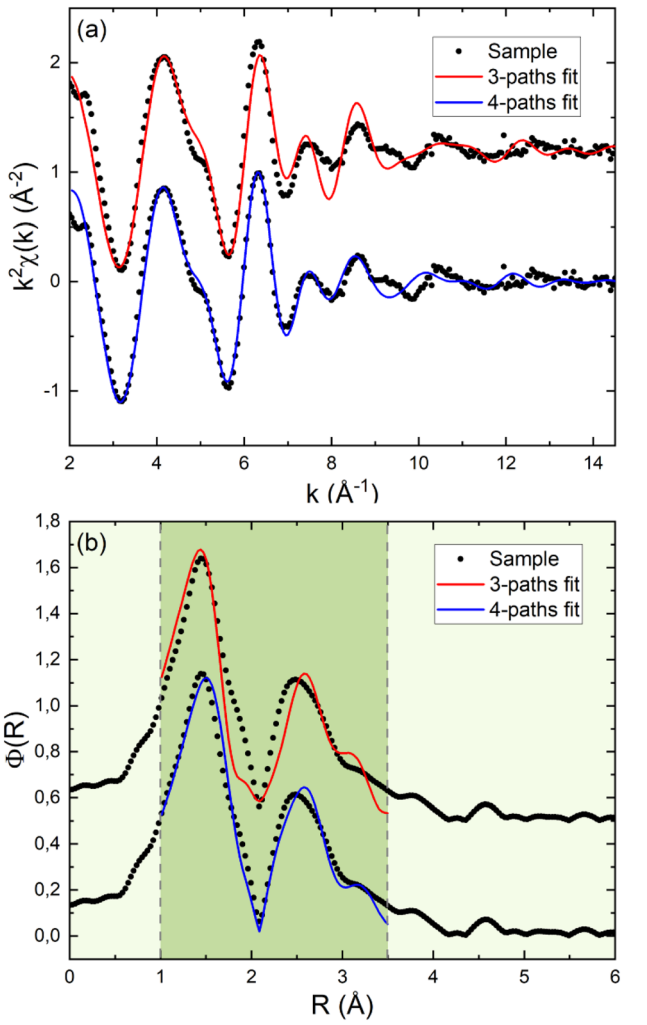

Fig. 4 (a) Room temperature k^2-weighted experimental EXAFS spectra and (b) the corresponding Fourier transform plot of the EXAFS signals shown in (a). Red and blue lines stand for a 3-path or 4-path fit, respectively.

$\Phi(R)$ presents three major peaks, the first of which, at $R = 1.5$ Å, corresponds mainly to a first oxygen coordination shell (Fe–O). The second one, at $R = 2.5$ Å, and the less intense third peak, at 3.2 Å, are both related to iron–iron interactions (Fe–Fe) that can be attributed to the high proportion of maghemite in the sample. As noted above, maghemite is an iron oxide with a cubic inverse spinel crystal structure in which Fe^{3+} ions occupy both octahedral and tetrahedral sites. This arrangement creates alternating layers of these coordination environments, resulting in distinct local atomic configurations.

The contribution of the nearest neighbours to the EXAFS function was isolated by selecting the first peaks of the Fourier transform (1.0 Å $\leq R \leq$ 3.5 Å) and using the standard Fourier filtering technique. The filtered EXAFS spectrum [see Fig. 4(b)] thus obtained was then fitted to the EXAFS equation. According to the local environment of maghemite, we first considered the 3 paths corresponding to Fe–O, Fe–Fe and Fe–Fe [red line in Fig. 4(b)]. The fitting procedure was conducted by setting the interatomic distances of the paths based on the specifications given by A. Corrias *et al.*,[48] and F. Maillot *et al.*,[49] (see Table 1), while the coordination number was treated as an adjustable parameter.

The performed analysis resulted in a broad fit that failed to elucidate fine experimental features such as the shoulder observed at 1.8–1.9 Å, or the shifted energy positions of the peaks at 1.5 Å, 2.5 Å, and 3.2 Å [see Fig. 4(b)]. Furthermore, the coordination number extracted from the fits for the Fe–Fe coordination shells is reduced compared to the maghemite standard (especially for the last one – $R = 3.44$ Å, see Table 2). Once more these differences suggest the non-exclusivity of maghemite while reconfirming the coexistence of other Fe-phases in the sample, already indicated *via* the XANES analysis.

Table 1 Interatomic distances (R); coordination numbers (N) obtained from crystallographic data. The deviation of our results from the reported values in the literature is within a range of experimental error of ≈0.03 Å. The data shown in the table correspond to the first reference. Each reference is followed by the experimental temperature, T, and maximum k value, k_{max}

		Fe–O	Fe–C	Fe–Fe	Fe–Fe	Fe–Fe
Maghemite	R (Å)	1.92	—	—	2.99	3.44
	N	5.25	—	—	3.75	8.25
	Ref.	(80 K, 16 Å^{-1});[47] (10 K, 17 Å^{-1})[48]				
Cementite	R (Å)	—	2.1	2.48	2.87	—
	N	—	2.66	8	6	—
	Ref.	(RT, 10.5 Å^{-1})[49]				
γ-Fe	R (Å)	—	—	2.53	—	—
	N	—	—	12	—	—
	Ref.	Calculated from lattice parameter Fe–Fe 3.587(1) Å[24]				

Table 2 Interatomic distances (R) and coordination numbers (N) obtained from EXAFS fitting considering 3 and 4 path fittings

		Fe–O	Fe–Fe	Fe–Fe	Fe–Fe
3-Path	R (Å)	1.92	—	2.99	3.44
	N	5(1)	—	3.0(6)	2.9(6)
4-Path	R (Å)	1.98(1)	2.56(3)	3.02(2)	3.50(2)
	N	5(1)	0.8(2)	2.9(6)	2.0(4)

In fact, when allowing the independent fit of the interatomic distances, including an additional Fe–Fe path at 2.56 Å that may arise from the other residual phases in the sample [see blue line in Fig. 4(b)], the goodness of the fit significantly improves. Then, we observe a shift of the peak attributed to Fe–O from the expected $R = 1.92$ Å in maghemite to 1.98(1) Å. The obtained coordination number, $N_{Fe-O} = 5(1)$, is slightly lower than that expected from the maghemite standard ($N = 5.25$), but within the range of error. These differences could suggest the presence of the cementite phase and the existence of an Fe–C coordination at slightly larger distances (2.1 Å).[50] In the 4-path fit, an additional Fe–Fe was included to better reproduce the region around 2.5 Å. It should be noted that this coordination shell is common to both Fe_3C and γ-Fe phases (see Table 1). According to the values reported in the literature presented in Table 1, the assumed percentages of the different phases and eqn (S1) and (S2) in the SI section, we might expect values of $R_{Fe-Fe} = 2.49$ Å and a coordination number of $N_{Fe-Fe} = 1.08$. However, the obtained values using the EXAFS fit [$R_{Fe-Fe} = 2.55(3)$ Å and $N_{Fe-Fe} = 0.8(2)$] do not really coincide with the coordination numbers of the Fe_3C or γ-Fe phases.

In accordance with the coexistence of different Fe-phases, the next Fe–Fe path is shared by maghemite and cementite. The expected values are $R_{Fe-Fe} = 2.97$ Å and $N_{Fe-Fe} = 3.98$ in contrast to those obtained from the fit: $R_{Fe-Fe} = 3.02(3)$ Å and $N_{Fe-Fe} = 2.9(6)$. Moreover, the last coordination shell is located in the R_{Fe-Fe} range at around 3.5 Å. This path is exclusive to the maghemite phase, as it does not appear in the other compounds (see Table 1). The coordination number obtained by fitting the experimental spectra is $N_{Fe-Fe} = 2.0(4)$, which is significantly lower than the expected value considering a maghemite percentage of 87% ($N_{Fe-Fe} = 7.18$).

In summary, although the 4-path model is noticeably better than the one that considers only 3-paths, there are some remaining problems arising from relating the experimental EXAFS data and the referred fitting that are evident above $k = 9$ Å^{-1} [see Fig. 4(a)]. These discrepancies could be due to the combination of several factors: (i) Fe_3C and γ-Fe show similar coordination shells, complicating their individual resolution; (ii) the expected percentages sometimes fall within the error range of the analysis method; and/or (iii) the maghemite NPs, with an average size of ~9(2) nm, present a significant fraction of surface atoms, where local disorder becomes relevant. This surface disorder can reduce the structural coherence required to reproduce fine oscillations at high-k values. Note that contributions from higher coordination shells may also exist; however, their detection in this system is likely limited due to signal damping and increased disorder. The current analysis focuses on the first three to four coordination shells ($R \leq 3.5$ Å), which fall within the reliable experimental range. Consequently, residual misfits in the high-k region are expected and reflect the intrinsic complexity of the sample's multiphase and nanoscale nature.

^{57}Fe Mössbauer spectrometry

^{57}Fe Mössbauer spectra recorded at 300 and 77 K are shown in Fig. 5. At 300 K, each spectrum consists of a dominant asymmetrical quadrupolar doublet in the centre, superimposed on non-well defined magnetic components. This situation is the reverse at 77 K, presenting a dominant magnetic feature with broadened lines superimposed on a central asymmetrical quadrupolar doublet. The best description of these two spectra requires at least 4 components, with the corresponding refined values of the hyperfine parameters being given in Table 3.

The main component resulting from a quadrupolar doublet at 300 K, which splits into a magnetic sextet and a minor quadrupolar doublet at 77 K, is characterized by an isomer shift value unambiguously attributed to the presence of Fe^{3+} species, *i.e.* Fe oxides. It is important to highlight that at 300 K, two quadrupolar subspectra were considered, but at 77 K a broad distribution of hyperfine fields is needed to better describe the hyperfine structure (which explains the mean values reported in Table 3). In addition, the magnetic features at 300 K were well described with two different magnetic sextets, whose values of hyperfine parameters made it possible to clearly attribute these components to the Fe_3C phase,[44] and the α-Fe phase. In fact, the two sextets observed can be attributed to iron atoms in two distinct crystallographic environments of the Fe_3C phase as well

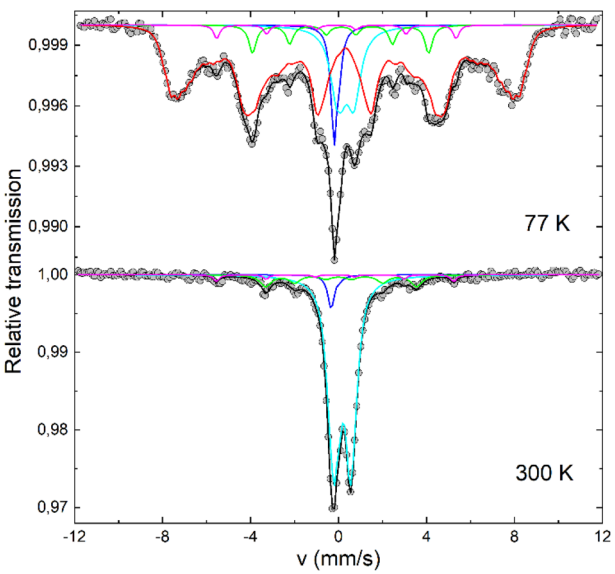

Fig. 5 Mössbauer spectra together with the fit obtained at $T = 300$ K and $T = 77$ K. The grey dots and the solid black lines represent the experimental data and the fit, respectively. Different sub-spectra corresponding to Fe-oxides (red sextet and cyan doublet), Fe_3C (green sextet), γ-Fe (blue singlet) and α-Fe (magenta sextet) phases have been considered.

Table 3 Refined values of hyperfine parameters estimated from the analysis of Mössbauer spectra at 300 and 77 K.; δ is the isomer shift with respect to α-Fe; Γ is the line width (width at half height); Δ is the quadrupolar splitting; 2ε is the quadrupole shift; and B_{HF} is the hyperfine field. The proposed phase identification and their relative proportions are also given

T (K)	δ (mm s^{-1}) $\pm$ 0.01	Γ (mm s^{-1}) $\pm$ 0.02	Δ or 2ε (mm s^{-1}) $\pm$ 0.01	B_{HF} (T) $\pm$ 0.05	Area (%) $\pm$ 2	Phase
300 K	−0.12	0.37	0.00		5	γ-Fe
	0.33	0.49	1.15		15	Fe oxides
	0.33	0.53	0.64		66	
	0.23	0.61	0.02	21.0	11	Fe_3C
	0.02	0.30	0.00	33.2	3	α-Fe
77 K	0.01	0.36	0.00		5	γ-Fe
	⟨0.45⟩		⟨0.04⟩	⟨37.6⟩	74	Fe oxides
	0.48	0.75	0.65		13	
	0.27	0.40	−0.02	24.6	6	Fe_3C
	0.07	0.32	0.00	33.5	2	α-Fe

as to the presence of a small amount of the α-Fe phase. The assignments for the Fe_3C phase are consistent with its orthorhombic crystal structure, in which iron atoms occupy two nonequivalent sites, each giving rise to slightly different hyperfine parameters due to variations in their local environments. The hyperfine field values and isomer shifts extracted from our measurements are in good agreement with those reported in the literature for both bulk and nanoscale cementite.[44] Finally, the asymmetry of the central part is satisfactorily described by the addition of a single line component unambiguously attributed to the paramagnetic γ-Fe phase, from the value of the isomer shift.[24] The relative proportions estimated at 300 and 77 K are in good agreement.

From this first analysis, we can conclude that the Fe^{3+} oxide phase is related to the presence of maghemite nanoparticles from the zero values of quadrupolar shifts, which significantly differ from those of magnetite, hematite, or iron hydroxides (*i.e.* goethite). These maghemite NPs show complete SPM behaviour at 300 K, but the distribution of hyperfine fields observed at 77 K is consistent with the small sizes of the NPs (magnetically unblocked or partially blocked). It would be preferable to consider two Fe^{3+} components attributed to the tetrahedral and octahedral sites, but the complexity of the hyperfine structure does not allow for drawing precise conclusions: only Mössbauer measurements in the presence of an external magnetic field could enable such proportions to be estimated. Moreover, small differences in the isomer shift are observed between 300 K and 77 K for Fe probes in the Fe_3C and α-Fe phases: the reduction is probably due to temperature-induced pressure effects.

The percentage of Fe oxides, Fe_3C and γ-Fe is consistent with the values estimated from XANES. However, the possible presence of 3% of α-Fe, suggested by Mössbauer analysis, could be barely distinguishable by XANES spectroscopy, although it is compatible with the results obtained by EXAFS since α-Fe exhibits a coordination shell similar to that of Fe_3C.

Magnetic properties

The measurement of the temperature dependence of magnetization between 2 and 340 K under a magnetic field of 100 Oe in the ZFC, FC and FH regimes [Fig. S2(a)] first shows that $M_{FC}(T)$ and $M_{FH}(T)$ are indistinguishable as expected for magnetic monodomains. On heating the sample above $T = 2$ K, magnetization increases and the $M_{ZFC}(T)$ curve exhibits a broad maximum centred around 65 K. This maximum is conventionally taken as the blocking temperature (T_B) associated with superparamagnetic NPs. This value, $T_B \approx 65$ K, is consistent with a system of small maghemite NPs with average diameters of around 9 nm. Using the value of the magnetic anisotropy for nano-maghemite and the known particle size, the T_B can be easily estimated using the well-known relation $25k_BT_B = kV$, leading to ~52 K. The $M_{ZFC}(T)$ curve does not decrease drastically above T_B, in agreement with a system of magnetic NPs with a size distribution. Moreover, the largest NPs remain blocked even at room temperature, as the $M_{ZFC}(T)$ curve is not zero. These features were also observed on the ZFC–FC–FH curves measured under higher magnetic field values [see Fig. S2(b)]. The temperature derivative of the M_{FC}–$M_{ZFC}(T)$ curves presents a maximum that corresponds approximately to the inflection point of the $M_{ZFC}(T)$ curves below $\langle T_B \rangle$.

The $M_{FC}(T)$ curve increases on cooling from 340 down to 2 K and shows a cusp at low temperature that is typically reported for SG states,[51] and suggests that the spins of the NPs could be blocked at low temperature. Finally, the lack of reversibility between the $M_{ZFC}(T)$ and $M_{FC}(T)$ curves that persists even at 300 K is surprisingly uncharacteristic of superparamagnetic NPs and could be related to the presence of a small amount of cementite NPs, which is characterized by open ZFC–FC curves.[44,52] This feature has been already observed in hollow maghemite NPs with highly disordered surface spins, and can be attributed to strong interparticle interactions and/or enhanced anisotropy in the system.[53] Therefore, an in-depth analysis of the dynamic relaxation processes of the system could help to understand the collective behaviour of our maghemite NPs.

Low-amplitude AC susceptibility curves were recorded between 2 and 300 K for six different frequencies of the H_{AC} (see Fig. 6). It can be observed from the $\chi'(T)$ curve that increasing the frequency, a temperature shift of the maximum, T_p, towards higher values occurs. This trend is commonly observed both in interacting SPM NPs and in SG-like systems.[54] To distinguish between them, a phenomenological parameter, Ω, which quantifies the peak shift per frequency decade

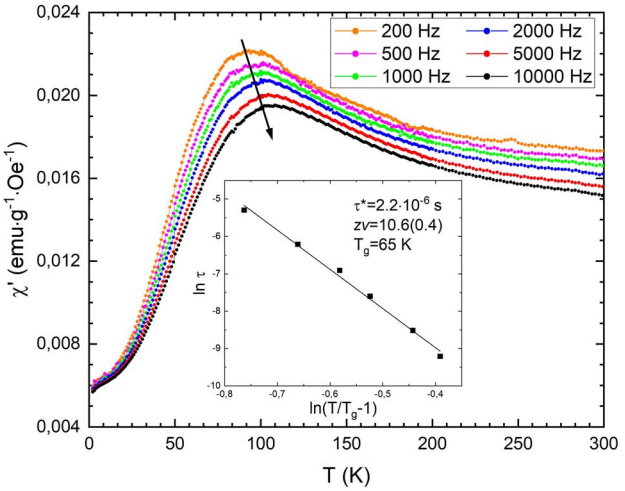

Fig. 6 Temperature dependence of the in-phase component of AC susceptibility (χ') at different frequencies. The black arrow points out the increasing trend of the temperature for the maximum as the frequency rises. The inset shows the fit to critical slowing down laws and the values obtained for their characteristic parameters.

$\left(\Omega = \frac{\Delta T_p}{T_p \Delta(\log_{10} f)}\right)$ can be calculated. This value gives a good criterion for distinguishing between canonical spin glass, SG-like and SPM regimes. Canonical spin glasses are poorly affected by frequency and thus, $\Omega = 0.005$–0.06 are typically reported.[53] However, values in the range $\Omega \sim 0.05$–0.13 are expected for magnetically coupled particles,[55] whilst those around 0.3–0.5 represent an ideal SPM system.[56] In our case, a value $\Omega \sim 0.09(0.02)$ is estimated, which is within the expected range for small interacting particles, similar to that previously reported for a system of superspin-glass maghemite NPs with intraparticle magnetic interactions,[55] $\Omega = 0.10$, and slightly above that reported for magnetite NPs with strong dipolar interactions, $\Omega = 0.032$.[57]

Therefore, it is tempting to discuss whether dipolar interactions between NPs may affect the overall behaviour of the χ_{AC} data displayed in Fig. 6. It is worth mentioning here that the magnitude of the χ'' component (not shown) does not increase with frequency, contrary to what is expected when strong dipolar interactions between NPs exist.[56,58] We might accordingly propose a non-interacting system of maghemite NPs, but this hypothesis can be further explored by studying the inverse of the ac frequency ($\tau = 1/f$) as a function of the temperature at which χ' peaks by means of the Arrhenius–Néel, Vogel–Fulcher and critical slowing down (CSD) laws. Attempts to fit using Arrhenius–Néel or Vogel–Fulcher laws yield unphysical values for the activation energy, suggesting a system of non-interacting NPs.

Hence, if we assume intraparticle magnetic interactions between an ordered ferrimagnetic core and a thin shell with canted spins, a divergence of the relaxation time τ is expected to occur at a SG-like transition temperature T_g. The temperature dependence of τ can be modelled using the following CSD law:[59]

$$\tau = \tau^* \left(\frac{T}{T_g} - 1\right)^{-zv}$$

where τ^* is the atomic spin-flip time of non-interacting superspin clusters which corresponds to slower characteristic relaxation times in the range of 10^{-6} to 10^{-9} s,[54,59,60] and zv is a dynamic critical exponent with typical values between 4 and 12 for conventional SGs.[54] Fitting our data to this CSD law gives a good fit (see the inset in Fig. 6) with a τ^* value $\sim 2.2 \times 10^{-6}$ s consistent with the relaxation times of SGs, $T_g \approx 65$ K, in good agreement with the peak location in the $M_{ZFC}(T)$ curve (see Fig. S2 in SI), and $zv \sim 10.6$. This value of the critical exponent is within the typical range for SG systems and similar to the values already reported for maghemite NPs (10–11),[53,59,61] and being close to that for diluted Fe–C NPs (9.5).[62] On the basis of this analysis, the existence of a critical slowing behaviour and the presence of a phase transition to a SG-like state thus seem to be responsible for the dynamics of our sample, reinforcing the idea that dipolar interactions between NPs in the SPM state alone could not explain both the AC and DC magnetic data.

A different approach, called the memory effect protocol, provides a better understanding of low-temperature dynamics. In Fig. 7, three different magnetization *versus* temperature curves are shown, (i) in black, $M_{is}(T)$, obtained during cooling with intermittent stops; (ii) in red, $M_{mem}(T)$, measured during warming up; and for comparison, (iii) in blue, $M_{ref}(T)$, the curve measured continuously during FC without any stop. During temporary stops, the field is switched off to allow the magnetization to relax downwards and, after each stop, 100 Oe are reapplied to resume the cooling process.

Throughout the intermittent stops, magnetization drops because the magnetic moments equilibrate in zero field and consequently $M_{is}(T)$ produces the observed step-like curve. It is worth noting that this characteristic also depends on the temperature at which the stop is carried out. For example, magnetization is restored almost completely after intermittent stops at 100 and 80 K, but noticeable differences appear after stops at 60, 40 and 20 K (see Fig. 7). This is because the magnetization depends on how quickly the moments realign in

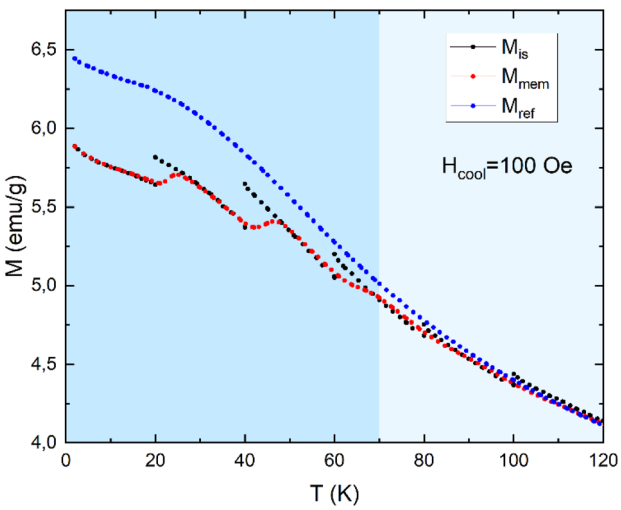

Fig. 7 Magnetic memory effect experiment with $H_{cool} = 100$ Oe: intermittent-stop cooling magnetization M_{is}, warming memory curve M_{mem} and field-cooling reference curve M_{ref} (see text for details).

response to the magnetic field.[54] In SG systems, if the stop is made near the freezing temperature, the dynamics is too slow for magnetization to recover easily after the waiting period. Consequently, large steps shown by the magnetization below 60 K suggest a disordered magnetic state. This value roughly coincides with the SG-like transition temperature, $T_g \approx 65$ K, previously obtained using the power law analysis and the maximum of the $M_{ZFC}(T)$ shown in Fig. 6 and S2, respectively.

Another remarkable result is the $M_{mem}(T)$ curve obtained during reheating (see Fig. 7), which also shows steps at exactly 20 and 40 K, and another, less notable step at 60 K. Consequently, the system restores the lower energy magnetic configuration established by the redistribution of energy barriers during the cooling process.[64] In other words, the system remembers its thermal history when the temperature is reestablished, thus implying "a memory effect", commonly displayed by systems in SPM as well as SG states. However, memory effects under the ZFC protocol are unique to spin glasses,[63,64] reinforcing our previous findings.

In addition, we analysed the magnetic relaxation of the system using the following procedure: after cooling the sample under a zero-field-cooling protocol from 300 down to 30 K, the magnetization is measured continuously for 3 hours (t_1) at $T =$ 30 K under an applied field of 100 Oe, then the temperature is reduced to 20 K and the magnetization is measured for 3 hours (t_2), and finally, the sample is then reheated to 30 K, measuring the magnetization for 3 hours (t_3). When the field is switched on for the first time at 30 K, after an immediate jump, the magnetic moments align gradually themselves towards the field direction and the magnetization grows logarithmically. During t_2, relaxation becomes very weak, and magnetization remains almost constant. When the temperature is restored to 30 K, magnetization returns to the value reached before temporary cooling. Moreover, the relaxation curve during t_3 is a continuation of the curve during t_1, as can be seen in the inset of Fig. 8. These results confirm the low-temperature memory effects and prove the argument that relaxation at low temperatures has no influence on the magnetic state at higher temperatures.[65]

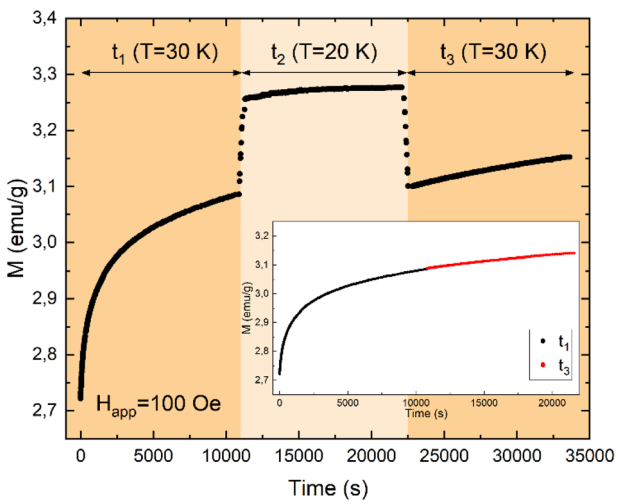

Fig. 8 Magnetic relaxation with an applied magnetic field $H = 100$ Oe after zero-field cooling to 30 K (t_1), reducing the temperature to 20 K (t_2) and reheating to 30 K (t_3). The inset plots 30 K relaxation data only, showing that the relaxation curve during t_3 is a continuation of the curve during t_1.

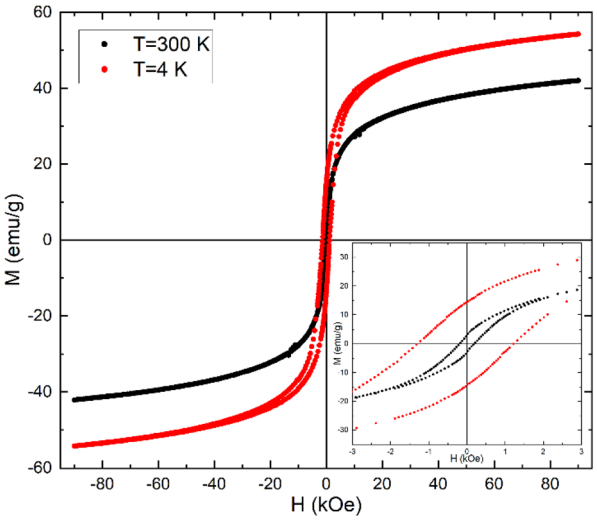

Fig. 9 $M(H)$ curves measured under ZFC conditions at $T = 300$ K (black) and $T = 4$ K (red). The inset shows an enlarged view of the central part of the loops.

In Fig. 9, the magnetization *versus* magnetic field curves, $M(H)$, recorded at $T = 4$ and 300 K are depicted. The fact that the $M(H)$ curve displays hysteresis at 300 K (see the enlarged view in Fig. 9), with $H_c \sim 190$ Oe and $M_r \sim 3$ emu g^{-1}, together with the absence of overlapping in the whole temperature regime of the M_{ZFC} and $M_{FC}(T)$ curves (see Fig. S2 in SI), implies that the system has not reached a fully SPM regime. Both features are probably related to the presence of cementite with a higher value of magnetic anisotropy.[44,52] Additionally, as can be seen in Fig. 9, the magnetization is not yet saturated even for ±85 kOe at 300 K, a clear signature of the existence of a disordered magnetic spin configuration at the NP surface. The values of M_s are slightly larger than those reported in the literature,[66] $M_s \sim 50$ emu g^{-1} at 4 K, but $\frac{M_r}{M_s} < 0.5$, thus suggesting that the Stoner–Wohlfarth criterion for blocked spins at low temperatures is not fully satisfied.[67]

On the other hand, the $M(H)$ curve measured at $T = 4$ K after cooling under ZFC conditions exhibits a larger coercive field, H_c, value and is symmetric around the origin (see the inset in Fig. 9). However, upon cooling the sample from room temperature to 4 K with a cooling field, $H_{cool} > 0$, the $M(H)$ curve shifts horizontally to the left (see Fig. S3 and S4 for the whole set of measured hysteresis loops) indicating the presence of a unidirectional anisotropy, known as the exchange bias effect (EB). The values of $H_c(T)$ and $H_{EB}(T)$ obtained from the $M(H)$ curves under a constant $H_{cool} = 5$ kOe are shown in Fig. 10(a). Coercivity reaches a value around 1400 Oe at low temperature and decreases with temperature, consistent with the onset of a disordered and frozen regime of the system. In turn, the value of H_{EB} falls down with increasing temperature and vanishes for

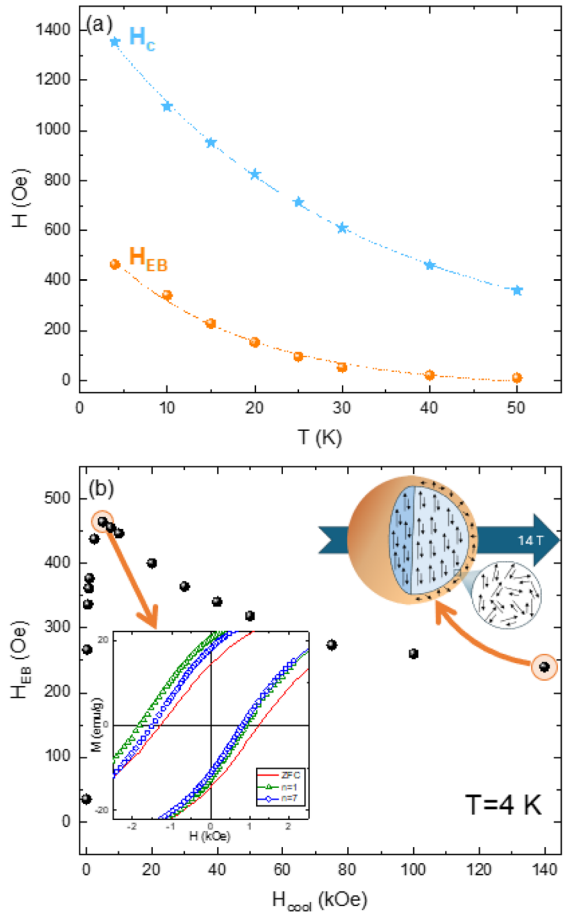

Fig. 10 (a) Temperature dependence of H_{EB} (orange points) and H_c (blue starts) with a cooling field of 5 kOe. (b) Cooling field dependence of H_{EB} at $T = 4$ K. The inset shows the central part of the $M(H)$ loops with $H_{cool} = 5$ kOe (green symbols) and after seven cycles (blue symbols) compared with that measured under ZFC conditions (red curve). A schematic representation of the core/shell magnetic structure is also depicted in the upper right part (see text for additional details).

$T > 50$ K, which roughly matches with the already estimated SG-like transition temperature $T_g \approx 60$ K. Furthermore, the best phenomenological model to explain the $\chi'(T)$ and $\chi''(T)$ curves is considering NPs with only intraparticle magnetic interactions. Thus, the strong magnetic coupling on maghemite NPs, *i.e.* between the disordered magnetic spins at the surface and the ferrimagnetic core of the NPs, is responsible for the observed EB effect.

The dependence of H_{EB} on H_{cool} at $T = 4$ K shows a rapid initial increase up to a maximum value $H_{EB} = 460$ Oe for $H_{cool} = 5$ kOe and then drops asymptotically to a value of around 250 Oe for an increase in $H_{cool} = 140$ kOe [see Fig. 10(b)].

Finally, it is worth noting that the magnetic coupling between the spins of the disordered surface and those of the core is robust enough to maintain the exchange-bias effect ($H_{EB} \sim 250$ Oe) under cooling fields as high as $H_{cool} = 140$ kOe, contrary to that reported for other core/shell systems, in which this effect disappears under lower cooling fields.[27,68] Moreover, the training effect of the exchange bias was analysed by measuring seven consecutive hysteresis loops after cooling the sample to $T = 4$ K with $H_{cool} = 5$ kOe. In the inset of Fig. 10(b), we show the first and seventh loops compared with those recorded under ZFC conditions. Although the value of H_{EB} slightly decreases after several cycles, it does not vanish, maintaining an almost constant value of about 350 Oe. This feature clearly indicates that the magnetic coupling between the spins at the core and the shell of maghemite NPs [see schematic representation of the core/shell magnetic structure in Fig. 10(b)] plays a relevant role in understanding the magnetic response of this system. Although direct compositional analysis of the nanoparticle surface was limited, indications from EXAFS and magnetic measurements suggest partial disorder and possible carbon or oxygen-rich surface layers resulting from interactions with the carbon matrix or synthesis conditions. These surface effects likely contribute to the observed spin-glass-like behavior, exchange bias, and memory effects.

Summary and concluding remarks

We have investigated the magnetic behaviour of a system that consists of quasi-spherical NPs of maghemite with a mean diameter of 9 nm. XANES and ^{57}Fe Mössbauer spectrometry confirm that maghemite is the majority phase ($\approx$87%), although small percentages of cementite (Fe_3C) and metallic Fe are also present. The formation of the other phases could be explained due to the interstitial incorporation of carbon atoms into the FCC lattice as we have already reported.[24] Even though sucrose could not be graphitized on the Fe NP surface as in similar Ni nanostructured systems,[25] this excess of carbon could be responsible for the appearance of Fe_3C.

Moreover, the magnetic behaviour of the sample is driven by the maghemite NPs, while the existence of a small amount of Fe_3C only affects the shape of the magnetization *versus* temperature curves measured after the ZFC and FC protocols. The estimated mean blocking temperature is in line with that expected for a broad size distribution centred around 9 nm. In fact, the magnetic dynamics of the sample indicates the presence of a phase transition to a SG-like state ($T_g \approx 65$ K). Memory effect and magnetic relaxation measurements point towards a highly disordered magnetic state and a frozen regime on the surface spins of maghemite NPs. The latter is responsible for the low temperature exchange-bias effect, which is robust enough to survive under magnetic cooling fields of up to 140 kOe, thus revealing high anisotropic intraparticle magnetic coupling between the spins at the core and shell of maghemite NPs.

Author contributions

M. G. V. conceptualization, investigation, data curation, methodology and formal analysis, writing original draft; M. P. F.-G., L. M., N. Y., D. M.-B., A. A. & J. M. G. data curation, and formal analysis; M. S. & A. B. F. sample preparation; P. G. & J. A. B. conceptualization, methodology, supervision, funding

acquisition. All the authors participated in the writing of the final version.

Conflicts of interest

There are no conflicts to declare.

Data availability

The data supporting this article have been included in the paper and in the SI.

X-ray diffraction patterns together with additional magnetic measurments can be found in the SI file. See DOI: **https://doi.org/10.1039/d5na00493d**.

Acknowledgements

This work has been partially supported by the following projects: (a) CI-MCINN-24-PID2023-150968OA-I00 & MCINN-23-PID2022-138256NB-C21 from AEI (Spanish Research Agency) and ERDF, UE; (b) SEK-25-GRU-GIC-24-113 from SEKUENS (Research Agency of the Principality of Asturias). L. M. thanks the Horizon Europe Programme for the financial support provided through a Marie Sklodowska-Curie fellowship (101067742). A. A. acknowledges her Ramón y Cajal grant received from the Spanish Ministry of Science and Innovation (RYC2022-038426-I). The authors thank Dr Lusegen A. Bugaev and Dr Olivier Mathon for providing XANES spectrum of the iron cementite standard and A. Vallina (SCTs, Universidad de Oviedo) for technical support in preliminary low-resolution TEM inspection.

Notes and references

1 S. Caspani, F. J. Fernández-Alonso, S. M. Gonçalves, C. Martín-Morales, B. Cortes-Llanos, B. J. C. Vieira, J. C. B. Waerenborgh, L. C. J. Pereira, A. Apolinario, J. P. Araújo, M. V. Gómez-Gaviro, V. Torres-Costa, M. J. M. Silván and C. T. de Sousa, *ACS Appl. Mater. Interfaces*, 2025, **17**, 16602.
2 F. Fernández-Álvarez, G. García-García, G. R. Iglesias and J. L. Arias, *J. Magn. Magn. Mater.*, 2024, **589**, 171574.
3 S. B. Attanayake, M. D. Nguyen, A. Chanda, J. Alonso, I. Orue, T. R. Lee, H. Srikanth and M. H. Phan, *ACS Appl. Mater. Interfaces*, 2025, **17**, 19436.
4 H. Gavilán, G. M. R. Rizzo, N. Silvestri, B. T. Mai and T. Pellegrino, *Nat. Protoc.*, 2023, **18**, 783.
5 S. Arsalani, E. J. Guidelli, M. A. Silveira, C. E. G. Salmon, J. F. D. F. Araujo, A. C. Bruno and O. Baffa, *J. Magn. Magn. Mater.*, 2019, **475**, 458.
6 S. Harvell-Smith, L. D. Tunga and N. T. K. Thanh, *Nanoscale*, 2021, **14**, 3658.
7 S. Ayyanaar, M. P. Kesavan, C. Balachandran, S. Rasala, P. Rameshkumar, S. Aoki, J. Rajesh, T. J. Webster and G. Rajagopal, *Nanomedicine*, 2020, **24**, 102134.
8 J. Peng, W. Zhang, L. Chen, T. Wu, M. Zheng, H. Dong, H. Hu, Y. Xiao, Y. Liu and Y. Liang, *Chem. Eng. J.*, 2021, **404**, 126461.
9 K. Q. Jabbar, A. A. Barzinjy and S. M. Hamad, *Environ. Nanotechnol. Monit. Manag.*, 2022, **17**, 100661.
10 X. Zhou, B. Bienvenu, Y. Wu, A. K. da Silva, C. Ophus and D. Raabe, *Nat. Commun.*, 2025, **16**, 2705.
11 D. S. Chaudhari, R. P. Upadhyay, G. Y. Shinde, M. B. Gawande, J. Filip, R. S. Varma and R. Zbořil, *Green Chem.*, 2024, **26**, 7579.
12 A. B. Fuertes, T. Valdés-Solís, M. Sevilla and P. Tartaj, *J. Phys. Chem. C*, 2008, **112**, 3648.
13 D. Zhang, S. Wei, C. Kaila, X. Su, J. Wu, A. B. Karki, D. P. Young and Z. Guo, *Nanoscale*, 2010, **2**, 917.
14 A. A. El-Gendy, E. M. M. Ibrahim, V. O. Khavrus, Y. Krupskaya, S. Hampel, A. Leonhardt, B. Büchner and R. Klingeler, *Carbon*, 2009, **47**, 2821.
15 D. Zhang, F. Xu, J. Lin, Z. Yang and M. Zhang, *Carbon*, 2014, **80**, 103.
16 D. Xie, Y. Chen, D. Yu, S. Han, J. Song, Y. Xie, F. Hu, L. Li and S. Peng, *Chem. Commun.*, 2020, **56**, 6842.
17 R. Sinclair, H. Li, S. Madsen and H. Dai, *Ultramicroscopy*, 2013, **134**, 167.
18 A. Kotoulas, C. Dendrinou-Samara, C. Sarafidis, T. Kehagias, J. Arvanitidis, G. Vourlias, M. Angelakeris and O. Kalogirou, *J. Nanopart. Res.*, 2017, **19**, 399.
19 E. Papadopoulou, N. Tetos, H. Gyulasaryan, G. Chilingaryan, A. Ginoyan, A. Manukyan, M. Angelakeris, M. Farle and M. Spasova, *Nano-Struct. Nano-Objects*, 2023, **34**, 100959.
20 N. Rinaldi-Montes, P. Gorria, D. Martínez-Blanco, A. B. Fuertes, L. F. Barquín, J. R. Fernández, I. De Pedro, M. L. Fdez-Gubieda, J. Alonso, L. Olivi, G. Aquilanti and J. A. Blanco, *Nanoscale*, 2014, **6**, 457.
21 N. Rinaldi-Montes, P. Gorria, D. Martínez-Blanco, A. B. Fuertes, I. Puente-Orench, L. Olivi and J. A. Blanco, *AIP Adv.*, 2016, **6**, 056104.
22 M. P. Fernández-García, P. Gorria, M. Sevilla, M. P. Proena, R. Boada, J. Chaboy, A. B. Fuertes and J. A. Blanco, *J. Phys. Chem. C*, 2011, **115**, 5294.
23 M. P. Fernández-García, P. Gorria, M. Sevilla, A. B. Fuertes, J. M. Greneche and J. A. Blanco, *J. Alloys Compd.*, 2011, **509S**, S320.
24 M. P. Fernández, D. S. Schmool, A. S. Silva, M. Sevilla, A. B. Fuertes, P. Gorria and J. A. Blanco, *J. Magn. Magn. Mater.*, 2010, **322**, 1300.
25 M. P. Fernández-García, P. Gorria, J. A. Blanco, A. B. Fuertes, M. Sevilla, R. Boada, J. Chaboy, D. Schmool and J.-M. Grenèche, *Phys. Rev. B: Condens. Matter Mater. Phys.*, 2010, **81**, 094418.
26 M. Fadel, F. J. Martın-Jimeno, M. P. Fernández-Garcıa, F. Suarez-Garcia, J. I. Paredes, J. H. Belo, A. Adawy, D. Martínez-Blanco, P. Álvarez-Alonso, J. A. Blanco and P. Gorria, *J. Mater. Chem. C*, 2023, **11**, 4070–4080.
27 M. H. Phan, J. Alonso, H. Khurshid, P. Lampen-Kelley, S. Chandra, K. S. Repa, Z. Nemati, R. Das, Ó. Iglesias and H. Srikanth, *Nanomaterials*, 2016, **6**, 221.

28 B. D. Cullity, *Introduction to Magnetic Materials*, Addison-Wesley, 1972.
29 J. M. D. Coey, *Phys. Rev.*, 1971, **27**, 1140.
30 D. Fiorani, A. M. Testa, E. Tronc, F. Lucari, F. D'Orazio and M. Nogués, *J. Magn. Magn. Mater.*, 2001, **226**, 1942.
31 X. Batlle, C. Moya, M. Escoda-Torroella, Ò. Iglesias, A. F. Rodríguez and A. Labarta, *J. Magn. Magn. Mater.*, 2022, **543**, 168594.
32 J. N. Nogués and I. K. Schuller, *J. Magn. Magn. Mater.*, 1999, **192**, 203.
33 N. Rinaldi-Montes, P. Gorria, D. Martínez-Blanco, A. B. Fuertes, L. Fernández Barquín, I. Puente-Orench and J. A. Blanco, *Nanotechnology*, 2015, **26**, 305705.
34 N. Rinaldi-Montes, P. Gorria, A. B. Fuertes, D. Martínez-Blanco, Z. Amghouz, I. Puente-Orench, L. Olivi, J. Herrero-Martín, M. P. Fernandez-Garcia, J. Alonso, M. H. Phan, H. Srikanth, X. Marti and J. A. Blanco, *J. Mater. Chem. C*, 2022, **10**, 1798.
35 G. C. Lavorato, E. Lima, H. E. Troiani, R. D. Zysler and E. L. Winkler, *Nanoscale*, 2017, **9**, 10240.
36 D. Tobia, E. Winkler, R. D. Zysler, M. Granada, H. E. Troiani and D. Fiorani, *J. Appl. Phys.*, 2009, **106**, 103920.
37 A. E. Berkowitz, W. J. Schuele and P. J. Flanders, *J. Appl. Phys.*, 1968, **39**, 1261.
38 V. Skumryev, S. Stoyanov, Y. Zhang, G. Hadjipanayis, D. Givord and J. Nogués, *Nature*, 2003, **423**, 850.
39 A. E. Berkowitz, J.-I. Hong, S. K. McCall, E. Shipton, K. T. Chan, T. Leo and D. J. Smith, *Phys. Rev. B: Condens. Matter Mater. Phys.*, 2010, **81**, 134404.
40 K. O'Grady, L. E. Fernandez-Outon and G. Vallejo-Fernandez, *J. Magn. Magn. Mater.*, 2010, **322**, 883.
41 P. Maltoni, *et al.*, *Adv. Compos. Hybrid Mater.*, 2024, **7**, 182.
42 G. Salazar-Alvarez, J. Qin, V. Šepelák, I. Bergmann, M. Vasilakaki, K. N. Trohidou, J. D. Ardisson, W. A. A. Macedo, M. Mikhaylova, M. Muhammed, M. D. Baró and J. Nogués, *J. Am. Chem. Soc.*, 2008, **130**, 13234.
43 P. Gorria, R. Boada, A. Fernández-Martínez, G. Garbarino, R. I. Smith, J. Chaboy, J. I. G. Alonso, D. Martínez-Blanco, G. R. Castro, M. Mezouar, A. Hernando and J. A. Blanco, *Phys. Status Solidi RRL*, 2009, **3**, 115.
44 H. Gyulasaryan, L. Avakyan, A. Emelyanov, N. Sisakyan, S. Kubrin, V. Srabionyan, A. Ovcharov, C. Dannangoda, L. Bugaev, E. Sharoyan, M. Angelakeris, M. Farle, M. Spasova, K. Martirosyan and A. Manukyan, *J. Magn. Magn. Mater.*, 2022, **559**, 169503.
45 B. Ravel and M. Newville, *Phys. Scr.*, 2005, **115**, 1007.
46 M. Wilke, F. Farges, P.-E. Petit, G. E. Brown and F. Martin, *Am. Mineral.*, 2001, **86**, 714.
47 M. L. Fdez-Gubieda, A. García-Prieto, J. Alonso and C. Meneghini, in *Iron Oxides: From Nature to Applications*, 2016, vol. 397.
48 A. Corrias, G. Ennas, G. Mountjoy and G. Paschina, *Phys. Chem. Chem. Phys.*, 2000, **2**, 1045.
49 F. Maillot, G. Morin, Y. Wang, D. Bonnin, P. Ildefonse, C. Chaneac and G. Calas, *Geochim. Cosmochim. Acta*, 2011, **75**, 2708.
50 S. Gražulis, A. Daškevič, A. Merkys, D. Chateigner, L. Lutterotti, M. Quirós, N. R. Serebryanaya, P. Moeck, R. T. Downs and A. Le Bail, *Nucleic Acids Res.*, 2012, **40**, D420.
51 M. Suzuki, S. I. Fullem, I. S. Suzuki, L. Wang and C. J. Zhong, *Phys. Rev. B: Condens. Matter Mater. Phys.*, 2009, **79**, 024418.
52 K. Lipert, J. Kaźmierczak, I. Pełech, U. Narkiewicz, A. Ślawska-Waniewska and H. K. Lachowicz, *Mater. Sci.-Pol.*, 2007, **25**, 2.
53 H. Khurshid, P. Lampen-Kelley, Ò. Iglesias, J. Alonso, M.-H. Phan, C.-J. Sun, M.-L. Saboungi and H. Srikanth, *Sci. Rep.*, 2015, **5**, 15054.
54 J. A. Mydosh, *Spin Glasses: an Experimental Introduction*, Taylor & Francis, London, 1993.
55 J. L. Dormann, R. Cherkaoui, L. Spinu, M. Noguès, F. Lucari, F. D'Orazio, D. Fiorani, A. Garcia, E. Tronc and J. P. Jolivet, *J. Magn. Magn. Mater.*, 1998, **187**, 139.
56 J. A. Ramos-Guivar, A. C. Krohling, E. O. López, F. Jochen Litterst and E. C. Passamani, *J. Magn. Magn. Mater.*, 2019, **485**, 142.
57 V. B. Barbeta, R. F. Jardim, P. K. Kiyohara, F. B. Effenberger and L. M. Rossi, *J. Appl. Phys.*, 2010, **107**, 073913.
58 G. T. Landi, F. R. Arantes, D. R. Cornejo, A. F. Bakuzis, I. Andreu and E. Natividad, *J. Magn. Magn. Mater.*, 2017, **421**, 138.
59 C. Djurberg, P. Svedlindh, P. Nordblad, M. F. Hansen, F. Bødker and S. Mørup, *Phys. Rev. Lett.*, 1997, **79**, 5154.
60 S. Chandra, H. Khurshid, W. Li, G. C. Hadjipanayis, M. H. Phan and H. Srikanth, *Phys. Rev. B: Condens. Matter Mater. Phys.*, 2012, **86**, 014426.
61 K. Nadeem, H. Krenn, T. Traussnig, R. Würschum, D. V. Szabó and I. Letofsky-Papst, *J. Appl. Phys.*, 2012, **111**, 113911.
62 M. F. Hansen, P. E. Jönsson, P. Nordblad and P. Svedlindh, *J. Phys.: Condens. Matter*, 2002, **14**, 4901.
63 M. Sasaki, P. E. Jönsson, H. Takayama and H. Mamiya, *Phys. Rev. B: Condens. Matter Mater. Phys.*, 2005, **71**, 104405.
64 K. H. Fischer and J. A. Hertz, *Spin Glasses*, Cambridge University Press, 1991.
65 Y. Sun, M. B. Salamon, K. Garnier and R. S. Averback, *Phys. Rev. Lett.*, 2003, **91**, 16.
66 P. G. Acevedo, M. A. González Gómez, Á. A. Prieto, J. S. Garitaonandia, Y. Piñeiro and J. Rivas, *Nanomaterials*, 2022, **12**, 456.
67 S. Morup, F. Bodker, P. V Hendriksen and S. Linderoth, *Phys. Rev. B: Condens. Matter Mater. Phys.*, 1995, **52**, 287.
68 L. Del Bianco, D. Fiorani, A. M. Testa, E. Bonetti and L. Signorini, *Phys. Rev. B: Condens. Matter Mater. Phys.*, 2004, **70**, 052401.